Materials and Design 199 (2021) 109383

Contents lists available at ScienceDirect

Materials and Design

journal homepage: www.elsevier.com/locate/matdes

Ultrafine microstructure and hardness in Fe-Cr-Co alloy induced by spinodal decomposition under magnetic field

Zhaolong Xiang [a,b,c], Lin Zhang [a], Yan Xin [c], Bailing An [a,b], Rongmei Niu [c], Masoud Mardani [c], Theo Siegrist [c,d], Jun Lu [c], Robert E. Goddard [c], Tiannan Man [a,b], Engang Wang [a,*], Ke Han [c,*]

[a] Key Laboratory of Electromagnetic Processing of Materials (Ministry of Education), Northeastern University, Shenyang 110819, China
[b] School of Materials Science and Engineering, Northeastern University, Shenyang 10819, China
[c] National High Magnetic Field Laboratory, Florida State University, Tallahassee 32310, FL, USA
[d] FAMU-FSU College of Engineering, Tallahassee, Florida 32310, USA

HIGHLIGHTS

- Variation of both microstructure and composition induced by spinodal composition was smooth at atomic scale.
- Magnetic field increased both amplitude and wave-length of spinodal composition.
- Magnetic field elongated α_1 domains lined up parallel to the direction of the magnetic field.
- Increased wave-length of spinodal composition resulted in decreased hardness and increased toughness.
- Mechanisms for fluctuations of composition and hardness were controlled by diffusion of certain alloying elements.

GRAPHICAL ABSTRACT

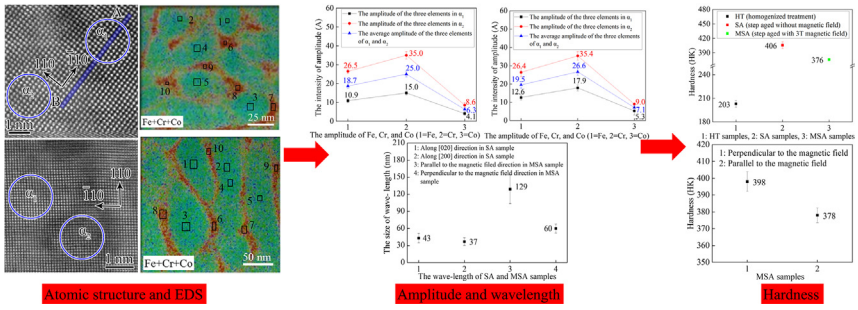

ARTICLE INFO

Article history:
Received 23 October 2020
Received in revised form 1 December 2020
Accepted 3 December 2020
Available online 9 December 2020

Keywords:
Fe-Cr-Co alloys
Spinodal decomposition
X-ray diffraction
STEM
EDS
Hardness

ABSTRACT

Application of an external magnetic field during heat treatment affects the hardness of magnetic Fe-Cr-Co alloys. The microstructure and composition at atomic scale, as well as the hardening mechanisms need extensive studies. Using atomic resolution STEM, we investigated the effect of a 3 T magnetic field on the spinodal decomposition, as well as microstructure and hardness in step-aged Fe27wt. %Cr15wt. %Co samples. Spinodal decomposition resulted in a homogeneous α phase transforming into an Fe-Co rich α_1 phase and a Cr rich α_2 phase. Although α_1 and α_2 showed distinct contrast at low magnification *Z*-contrast images, close examination at atomic scale of the samples showed no sharp α_1/α_2 interfaces. Inside each phase, composition fluctuations occurred. A 3 T external magnetic field during step aging increased the size of the α_1 phase and introduced microstructural anisotropy, which is desired for permanent magnet applications, In addition, the spinodal decomposition increased the hardness. Annealing in a 3 T magnetic field decreased the hardness but increased the ductility, which is desirable for manufacturing permanent magnets. The change in hardness values is attributed to the composition fluctuations of Fe, Cr and Co, and we further discuss the mechanisms for composition fluctuations and hardness.

* Corresponding authors.
E-mail addresses: egwang@mail.neu.edu.cn (E. Wang), han@magnet.fsu.edu (K. Han).

https://doi.org/10.1016/j.matdes.2020.109383

1. Introduction

Spinodal decomposition occurs in certain alloys when the alloy is heated to a range of temperatures where the two phases become immiscible. This range appears in phase diagrams as a miscibility gap. When spinodal decomposition occurs, the elements of the alloy separate, causing lattice mismatch that generates coherent internal stress, leading to an increase in hardness [1].

FeCrCo permanent magnet alloys are known for their excellent plasticity, ductility, and machinability, making them suitable for use in small devices with accurate dimensions and complicated shapes, such as wires, tubes, bars, and strips [2,3]. Consequently, they are widely used in motors for electrical appliances [4], hybrid cars [5] and wind turbines [6].

The manufacturing of magnetic alloys usually requires heat treatment under external magnetic fields to enhance the magnetic properties. This practice was used, for example, in FeNdZrB [7], FePt [8–10], and FeCrCo alloys [11]. An external magnetic field during isothermal heat treatment can improve anisotropy of the α_1 phase and elongate it in a direction parallel to the applied magnetic field, resulting in enhanced magnetic properties [12]. However, the heat treatment affects not only the magnetic properties [13–15] but also the mechanical properties [16,17]. In particular, no research has been done so far on the hardening mechanism of Fe-Cr-Co treated in a magnetic field, but we can deduce the mechanism from that of other Fe-Cr alloys [18,19] that are all known to be spinodal. Researchers have studied, for example, Fe32at%Cr [20] and Fe52.85at%Cr [21] alloys. It is generally accepted that hardness results from spinodal decomposition, which leads to element fluctuations. In duplex stainless steel, for example, which is an alloy of consisting of an iron matrix and typically more than 10.5% chromium, the hardness was found to increase almost proportionally with the amplitude of the Cr concentration fluctuations after aging the alloy at 300–400 °C [22].

In order to evaluate the contribution of the spinodal decomposition to the increased strength, several groups used formulas to calculate the value of the strength increment. The amplitude and lattice mismatch between α_1 and α_2 phases play important roles in these calculations [18,23]. These two parameters can be obtained by measuring the composition and atomic microstructure of the two phases. Using the phase diagram of Fe31wt%Cr23wt%Co alloy, previous work deduced that the α phase decomposes after aging at 600 °C into an iron-cobalt rich α_1 phase and a chromium rich α_2 phase [24]. Other groups have confirmed this prediction in FeCrCoAl [25], FeCoCrWGa [26], and FeCrCoTiSi [27] alloys, using Mössbauer spectrometry. Conventional transmission electron microscopy (TEM) has been used to investigate the modulated microstructure of Fe-Cr-Co alloys. Using conventional TEM, we also analyzed the effect of grain boundaries on the microstructure of spinodal decomposition in FeCrCo made by directional solidification in a magnetic field [28,29]. Since spinodal decomposition occurs at the nanometer scale, however, TEM alone is insufficient for revealing the compositional variation of the α_1 and α_2 phases at a fine scale. A very effective technique for studying ultrafine-scale structures is atomic resolution high-angle-annular-dark-field scanning transmission electron microscopy (HAADF-STEM), as it can provide both atomic scale microstructure and atomic scale chemical composition analysis of α_1 and α_2 phases.

Magnetic fields have been used to improve modulated structure and enhance properties in FeCrCo alloys, such as FeCrCoMoTiNb [30] and FeCrCoMo [31]. The microstructure and composition at atomic scale, as well as the hardening mechanisms without and with external magnetic field, however, still remain largely unclear. In this study, we analyzed the hardening mechanism of spinodal decomposition by investigating the microstructure and composition at atomic scales using HAADF-STEM. We also analyzed the hardness of an Fe27wt%Cr15wt%Co alloy after step aging without and with a magnetic field of 3 T.

2. Experimental procedures and calculations

2.1. Sample preparation

We prepared an ingot of Fe27wt%Cr15wt%Co alloy by melting oxygen-free Fe (99.99 wt. %), high-purity Co (99.95 wt.%), and high-purity Cr (99.96 wt. %) in a CJB-150 vacuum electric arc furnace in hemispherical copper molds with inner diameter of 40 mm. From this ingot, we made samples of $10 \times 15 \times 5$ mm^3, with the long side along the cooling direction.

Three types samples HT (homogenized treatment), SA (step aged without magnetic field), and MSA (step aged with 3 T magnetic field) were studied. All samples were first homogenized treatment (HT) for two hours at 1300°C under Ar atmosphere. Subsequently, HT samples were examined under homogenized condition. SA and MSA samples were placed in the center of a vacuum resistance furnace under a high-field superconducting magnet, which can generate a magnetic field with a maximum magnetic flux density of 12 T at the center of a Φ100 mm cold bore. Then, the SA and MSA samples were step aged at 645°C for 1 h, 620°C for 1 h, 600°C for 2 h, 580°C for 3 h, 560°C for 4 h, 540°C for 5 h, 520°C for 6 h and furnace cooled without and with 3 T magnetic field, respectively. The placement of the MSA sample was such that its cooling direction during the casting was parallel to the direction of the field.

The phase constitutions of all three samples were examined by X-ray diffraction (XRD). Two specimens for later TEM and STEM examination were prepared by slicing thin sheets (each $10 \times 15 \times 0.5$ mm^3) from SA and MSA samples. These specimens were ground to a thickness of 30 μm. From each, a 3 mm diameter disk was punched out, then glued on a copper ring. The samples were then ion milled at 3–5 keV using an incidence angle of 5°-7°. In order to analyze the orientation relationship between the α_1 phase and external magnetic field, we marked the original external magnetic direction on the MSA samples when we cut the sample. We loaded the sample on TEM holder by aligning the magnetic field direction to the long axis of the sample holder. We only rotated "Y" direction to check the direction of the α_1 phase.

2.2. Analysis of XRD data

Phase data were collected by XRD, using a Scintag Theta-2-Theta reflection diffractometer with Cu Kα radiation (wavelength λ 1.540562 Å) and diffracted analyzer. We examined all Types samples in order to collect data on phases and lattice parameters. The scanning angle was set to move in one-second steps of 0.02° from 30° to 120°. In order to more accurately analyze the peak shift and separation in the (110), (200), and (211) directions, we changed the one-second step setting to 0.0025° and collected data from 43° to 46°, 63° to 66°, and 81° to 85°. We used standard Si powder to correct reflections.

In order to study the influence on lattice constant of step aging without magnetic field (in the case of SA samples) or step aging with 3 T magnetic field (in the case of MSA samples), we calculated lattice constants for (110), (200), and (211) (Figs. 3b-3d). We compared the fitting results from different approaches and reported θ value using Gaussian fit.

We calculated the volume fraction of α_1 and α_2 phases in SA samples from (211) direction using the following formula:

$$I_\alpha = \frac{K_1 W_\alpha}{\rho_\alpha \left\{ W_\alpha \left[\left(\frac{\mu}{\rho}\right)_\alpha - \left(\frac{\mu}{\rho}\right)_\beta \right] + \left(\frac{\mu}{\rho}\right)_\beta \right\}} \quad (1)$$

where I_α is integrated intensity per unit length of diffraction line, K_1 is a constant, ρ the density, W_α the weight fraction, and μ/ρ is the absorption coefficient (cm^2/g). The absorption coefficient of Fe, Cr, and Co are 304.4 (cm^2/g), 252.3 (cm^2/g), and 338.6 (cm^2/g), respectively. Using Energy Dispersive Spectroscopy (ESD) in STEM, we measured the composition

of α_1 and α_2 phases are about 68.9wt%Fe12.0wt%Cr19.1wt%Co, 31.5wt% Fe62.0wt%Cr6.4wt%Co, respectively. Using the composition ratio of Fe, Cr, and Co in α_1 and α_2, we calculated the absorption coefficient of α_1 and α_2 phases as 304.4 and 217.7, respectively, and the density of α_1 and α_2 phases as 7.94 (g/cm^3) and 7.50 (g/cm^3), respectively.

2.3. Analysis of microstructure

Using a JEOL-2011 transmission electron microscope (TEM) and a JEM JEOL-ARM200cF, we examined the step aged samples at 200 kV. For HAADF-STEM images, the spot size was 4c, condenser lens aperture was 40 μm and image scan speed was 32 pixels/μs. The beam convergence angle was 21 mrad, and the STEM image collection angle was from 68 mrad to 174 mrad. Using the Image Pro-Plus software, we measured the volume fraction of α_1 and α_2 phases.

We also used electron-energy-loss spectroscopy (EELS) to collect the core-loss spectra of Fe, Cr, Co, in order to calculate sample thickness. In this case, the beam convergence angle was 21 mrad and the EELS collection angle was 100 mrad. Each spectrum was acquired in 2 s using dual range EELS.

In addition, we analyzed changes in element composition between phases in Fe-Cr-Co by means of (EDS), using the Oxford Aztec system in STEM. In order to be sure that our EDS results were not affected by the thickness of the samples, we computed absolute thickness by using the EELS Log-Ratio technique [32].

We took a HAADF-STEM structure image of MSA sample and acquired an EELS spectrum from the image Fig. 1a. We used the $I_0 = I_t \exp(-t/\lambda)$ function in Digital Micrograph software to compute the thickness of region A in α_2 phase and region B in α_1 phase (Fig. 1b). We calculated the effective atomic number (Z_{eff}) in order to get the absolute thickness. The simplified formula for the effective atomic number, Z_{eff}, can be described as [33]:

$$Z_{eff} = \sqrt[2.94]{f_1 \times (z_1)^{2.94} + f_2 \times (z_2)^{2.94} + f_3 \times (z_3)^{2.94} + \ldots} \quad (2)$$

where f_n is the fraction of the total number of electrons associated with each element, and Z_n is the atomic number of each element. The composition of region A and region B were Fe27at%Cr19at%Co and Fe52at% Cr9at%Co, respectively, so the Z_{eff} for region A was 24.9, and the Z_{eff} for region B was 26. We then computed the thickness for region A as 103.1 nm and B as 103.7 nm, so close as to be substantially the same for our purposes.

We used an absolute integrator program and MATLAB to digitize the intensity of atomic columns of SA and MSA samples [34,35]. From our thickness calculation, the thickness of MSA sample is uniform, and the atomic number of Fe, Cr, Co are similar. We can assume each atomic column to have same number of atoms. We simulated the intensity of the atomic columns to analyze the composition of α_1 and α_2 phases.

2.4. Testing of hardness

Hardness tests were performed on a Tukon 2100 tester with a diamond indenter under a load of 0.5 kg for a dwelling time of 10 s. We used a Vickers indenter to obtain average hardness and a Knoop indenter to analyze the anisotropy in hardness of samples treated with a magnetic field.

3. Results and discussion

3.1. X-ray diffraction data

XRD data indicated that spinodal decomposition resulted in a body center-cubic (bcc) α phase being decomposed into an iron-cobalt rich bcc-α_1 and a chromium rich bcc-α_2 phases (Fig. 2). HT samples contained only the bcc-α phase with a single lattice constant, when the data was collected using a coarser step size (0.02°) (Fig. 2a). In step aged SA and MSA samples, however, data collected using a finer step size (0.0025°) revealed the presence of phase decomposition, although data collected using a coarser step size (0.02°) showed no significant phase change at all (Fig. 2). The (110) and (200) peaks for SA and MSA samples showed shifts towards smaller angles, slightly more in SA than in MSA. These shifts indicate that the lattice spacing is smallest in HT samples and largest in SA samples. The difference of lattice distance between SA and MSA in these directions, however, was marginal because the difference was smaller than the standard deviation (Table 1). By using XRD, some researchers detected the presence of sidebands or dual peaks at same direction in CuNiSn [36,37], CoFeO [38], TiNbTaZr [39], LaTiGaFeCoSb [40], TaMoAlN [41], and TiO-VO [42,43] systems. They concluded that this sidebands or dual peaks were caused by the spinodal decomposition. In our study, the (211) reflection for Types HT and MSA samples showed only a single peak, but SA samples had dual peaks, one with downward and the other upward shifts (Fig. 2b, c, d). We attribute these dual peaks to the presence of both iron-cobalt rich bcc-α_1 and chromium-rich bcc-α_2 phases. The lattice constant for the left peak (α_1) was 0.2878 ± 0.0002 nm, larger than HT samples, while the lattice constant for the right peak (α_2) was 0.2872 ± 0.0002 nm, smaller than HT samples (Table 1). We deduced that dual peaks are probable for the (110) and (200) reflections, even though they did not appear in our data. Our

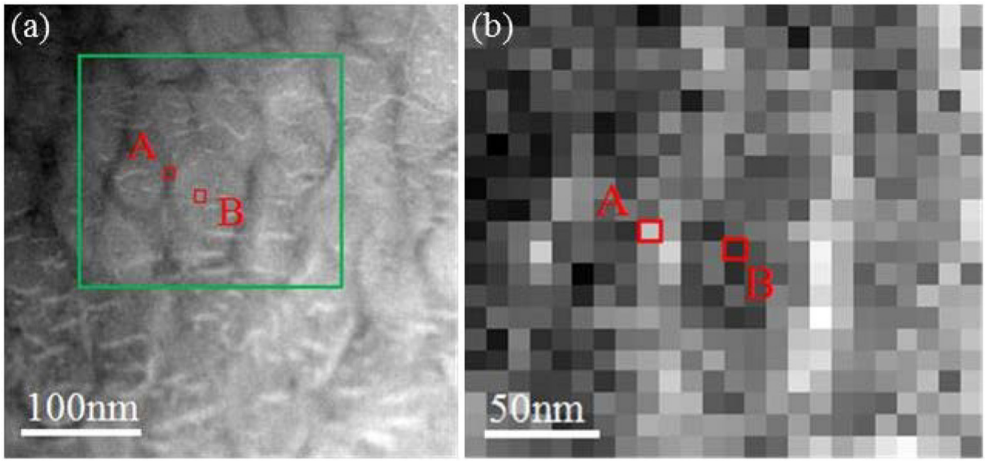

Fig. 1. Calculation of absolute thickness of MSA sample. (a) HAADF-STEM structure of MSA. (b) EELS spectrum of green rectangle region as shown in the image (a). We used EELS spectrum to compute the thickness of region A in α_2 phase and region B in α_1 phase.

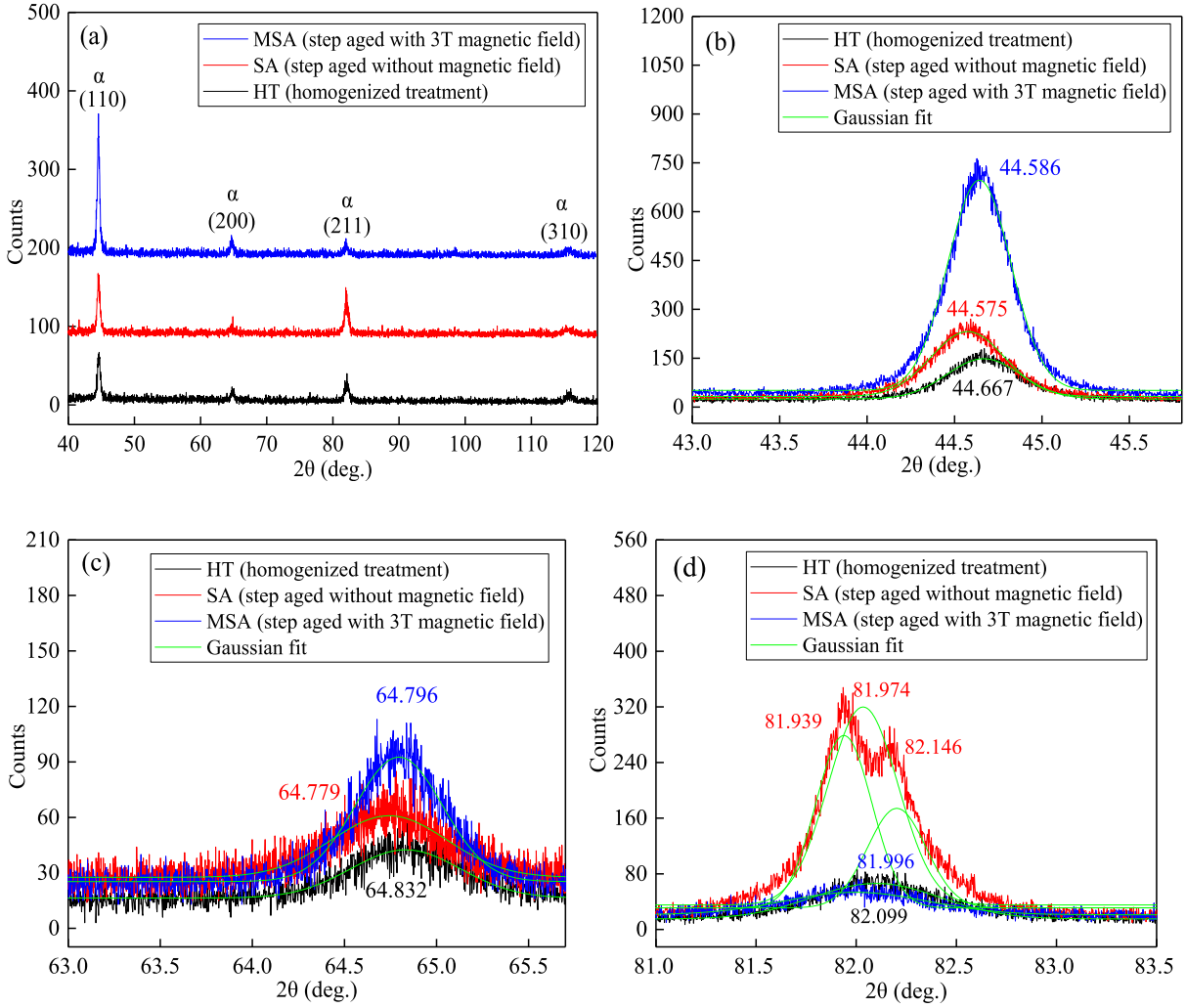

Fig. 2. X-ray diffraction patterns of the three Types samples from various scanning angles. (a) 40–120°. (b) 43–46°. (c) 63–66°. (d) 81–84°. In the (110) and (200) directions, XRD patterns show single peaks for all types samples, but in the (211) direction, SA samples shows peak splitting (d).

Table 1
Lattice constants of HT samples, SA samples, and MSA samples. Values were calculated using lattice spacing in (110), (200), and (211) directions.

Samples	a (110)	Error bar[a]	a (200)	Error bar	a (211)		Error bar
HT	0.2867	0.0002	0.2874	0.0003	0.2873		0.0001
SA	0.2873	0.0001	0.2876	0.0001	Left peak =0.2878	Right peak = 0.2872	0.0002
MSA	0.2872	0.0003	0.2875	0.0002	0.2876		0.0002

[a] Each type sample was tested three times. The error bars are the values of standard deviation of three results.

HAADF-STEM results confirmed that the lattice spacing in α_1 was greater than in α_2. We calculated the area ratio between the α_1 peak and the α_2 peak as about 1.4. Using the above formula (1), we estimate the volume fraction of α_1 and α_2 as 60% and 40%, respectively.

The relative intensity (110) in MSA samples was much higher than that in HT and SA samples, indicating that texture was introduced. This enhancement in texture was attributed to external magnetic field.

3.2. Microstructure

Our selected area diffraction patterns (SADPs) showed ellipsoid diffraction spots in step-aged samples (Fig. 3). The presence of these patterns indicated a modulated microstructure in which α_1 and α_2 had slightly different orientations and lattice constants, resulting in diffraction spots overlaying, but not quite atop each other. Similar overlapping diffraction spots were also found in Cu15Ni8Sn alloys [36,44]. Although this modulated structure has been widely studied in FeCrCoV [45], FeCrCoSi [46,47] alloys, so far no researcher has mentioned the presence of ellipsoid SADPs in these alloys after spinodal decomposition.

We used atomic resolution HAADF-STEM to investigate SA and MSA samples. When the modulated microstructure of α_1 and α_2 phases of SA was viewed along [001] direction, many bright patches of α_1 phase appeared throughout the surrounding α_2 dark matrix. In MSA sample, patches of the α_1 phase, which were more elongated than in SA, lined up parallel to the direction of the magnetic field. Since the atomic number of Cr is lower than that of either Fe or Co, we deduced that the α_2 matrix (dark network) was Cr-rich and that the α_1 phase (bright patch) was Fe and/or Co rich (Fig. 4a and b).

Applying a magnetic field increased both wavelength itself and the wavelength anisotropy of the spinodal decomposition in step-aged samples. In SA samples, the average wavelength (λ) was 43 ± 7.5 nm along the [020] direction and 37 ± 6.9 nm along the [200] direction. In MSA samples, the λ values parallel and perpendicular to the magnetic field direction were 129 ± 24.6 and 60 ± 7.1 nm, respectively. Application of a magnetic field therefore increased the λ ratio values from 1.2 in SA to 2.2 in MSA (Fig. 4).

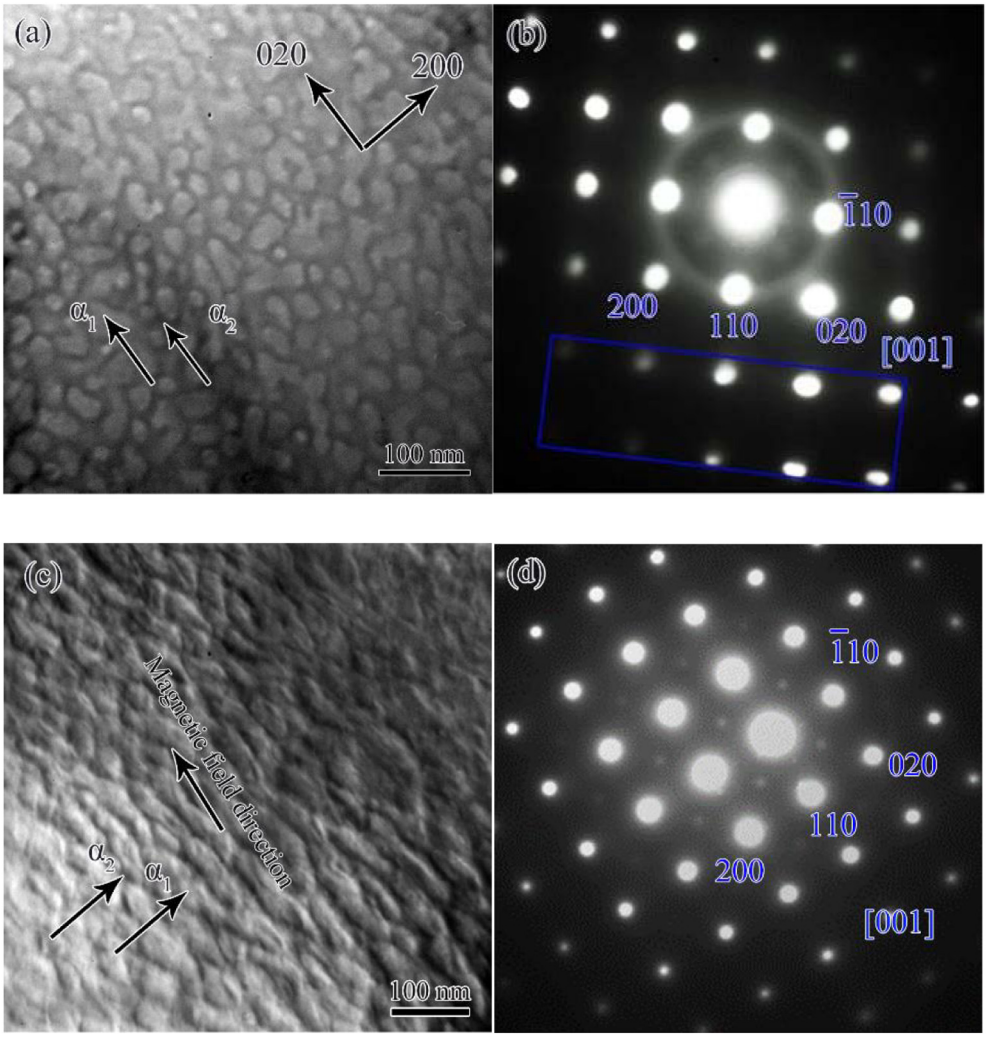

Fig. 3. TEM images of α_1 and α_2 phases in two samples. (a) Bright field image of SA sample, as viewed in the [001] direction. Spherical α_1 domains are uniformly distributed through α_2 network. (b) SADP image of SA sample. The diffraction points are elliptical, especially in the blue rectangle region, indicating the presence of two overlapping points in the same location. (c) Bright field image of MSA sample, as viewed in the [001] direction. Elongated α_1 domains are arranged along the magnetic field direction. (d) SADP image of MSA sample showing elliptical diffraction points similar to those seen in SA.

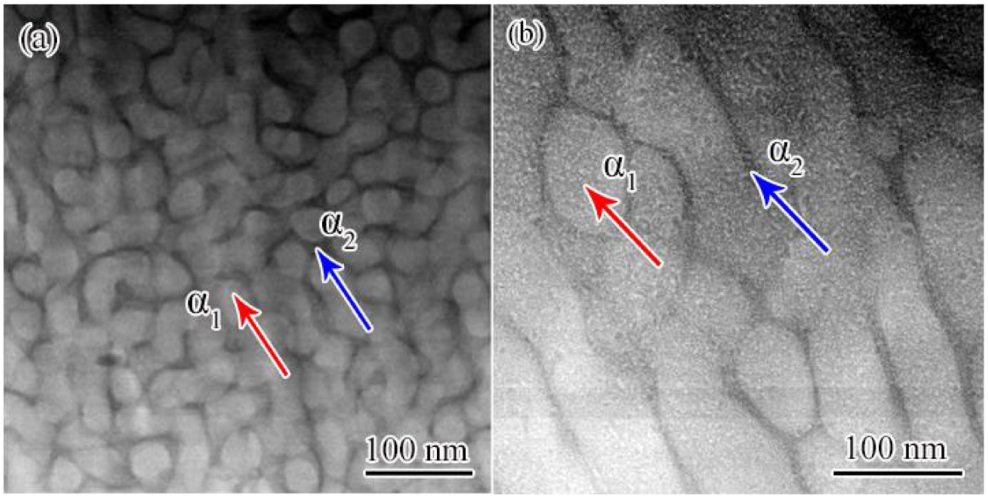

Fig. 4. Low magnification HAADF-STEM images of α_1 and α_2 phases of SA and MSA samples, as viewed along [001] direction. Fig. 4a. SA sample. Spherical α_1 domains (as indicated by red arrow) are uniformly distributed through the α_2 network (blue arrow). Fig. 4b. MSA sample. Many elongated α_1 domains (as indicated by red arrow) are uniformly distributed through the α_2 network (blue arrow) in direction parallel to the magnetic field.

The volume fraction of α_1, measured from HAADF-STEM images, showed that the application of a magnetic field during step aging increased the volume fraction of α_1 phase from 62% in SA samples to 72% in MSA samples. In SA samples, the volume fractions of α_1 and α_2 phases were 62% and 38%, respectively, confirming our previous XRD results (Figs. 4 and 2). Therefore, the application of magnetic fields accelerates the growth of the α_1 phase. This acceleration reflects the fact that this α_1 phase has a larger ferromagnetic moment than α_2 (Fig. 4).

The lattice constant in the Co/Fe-rich α_1 phase in SA and MSA samples, measured from HAADF-STEM images, was about 0.4% higher than in the Cr-rich α_2 phase (Table 2). The interfaces remained coherent; i.e., because of the low λ value, the small difference between the two lattice constants introduced no misfit dislocations (Fig. 5a and g).

Digitized image of SA samples did not reveal any sharp interfaces between α_1 and α_2, even though the intensity of atomic columns in the α_1 phase was, on average, 112% higher than in α_2 phase (Fig. 5a and d). Digitized atomic resolution images showed that the intensity was different in different regions of each phase, indicating that a variation in chemistry must have occurred inside both phases (Fig. 5b-c, e-f, and h-k).

Using atomic resolution HAADF-STEM images, we measured the lattice spacing in α_1 and α_2 phases in the [110], [−110], [010], and [100] directions for both SA and MSA samples, and we calculated the lattice constant in α_1 and α_2 phases in the four directions (Table 2) (also see Fig. 5a, g, and Appendix A). For SA, the average lattice constants of α_1 and α_2 phases were 0.2787 nm and 0.2775 nm, respectively. For MSA, the average lattice constants of α_1 and α_2 phases were 0.2759 nm and 0.2748 nm, respectively.

3.3. Composition

A combination of HAADF-STEM imaging, (EDS) mapping, line-scanning, and point analysis confirmed that the α_1 phase was rich in both Fe and Co and that the α_2 phase was rich in Cr (Fig. 6 and Table 3). The composition of Fe, Cr, and Co in both SA and MSA samples changed periodically, sometimes as a cosine wave and sometimes as a square wave function. This occurs mainly because of a pattern of uphill diffusion of Cr throughout the alloy. This pattern, in which one region is Cr rich and Fe-Co poor while the next is Fe-Co rich and Cr poor, is characteristic of all binary Fe-Cr alloys [1,48]. Researchers also found this pattern in other spinodal alloys, such as $Zr(Fe,Nb)_2$ [49], U-50Zr [50], and 5 wt% Alnico5 doped $Sm(Co_{0.9}Cu_{0.1})_5$ ribbons [51]. Our EDS-Mapping results showed that the intensity of Fe, Cr, Co changed gradually within both α_1 and α_2 phases -- the diffusion reaction was continuous. At the boundary between α_1 and α_2, however, the diffusion reaction was discontinuous in that the intensities of Fe, Cr, Co changed abruptly from one phase to the other. This result indicates that the reaction is still developing within each phase but mature at the boundary (Fig. 6c, f).

The amplitude level (A), which we defined as the maximum concentration minus the average concentration of a given element, was greater in the α_2 phase than in the α_1 phase for all three elements (Fe, Cr, and Co) (Fig. 7). In both phases, the value of A was highest for Cr and lowest for Co (Fig. 6b, e). The maximum A value for Cr was greater in MSA samples than in SA samples. The average λ for all three elements in MSA samples was also greater than in SA samples, showing that step aging with an external magnetic field promotes the diffusion of Fe, Cr, and Co atoms (Figs. 6 and 7).

The phenomenon of Fe and Co diffusing together while Cr diffuses in the opposite direction can be explained by excess Gibbs free energy ($(G_\upsilon)^E$), expressed as:

$$\left(G^{\upsilon}\right)^{E} = \Omega_{AB}\chi_A^{\upsilon}\chi_B^{\upsilon} \tag{3}$$

where Ω_{AB} is the interaction parameter for A-B regular solution. The two elements (A and B) attract each other when Ω_{AB} is negative and repel each other when Ω_{AB} is positive. It was found that Ω_{AB} values were 12 kJ/mol for Fe-Cr system and -12 kJ/mol for Fe-Co [52]. In our alloy, therefore, Fe and Co are miscible but Fe and Cr are not. Cr was rejected from both Fe-rich phases, which was also rich in Co.

3.4. Hardness

Spinodal decomposition hardening was also studied in AlMg [53] and MnCuNiFe [54] alloys. Our Vickers hardness tests of HT, SA, and MSA samples indicated that hardness increased with step aging, more in the SA sample (step aged without magnetic field) than in the MSA (step aged with 3 T magnetic field) (Fig. 8a). The Knoop hardness value for MSA sample was 398 HV, greater when the indenter was perpendicular to the magnetic field than when parallel (Fig. 7b). We also tested the Knoop hardness of a HT sample and a SA sample. The results were shown in appendix B.

Hardness in FeCrCo alloys is often assumed to be closely related to wavelength and amplitude, i.e. periodic composition change. This change is widely accepted that results from spinodal decomposition that results from step aging (Fig. 6). This type of change increases hardness by introducing a lattice mismatch, which generates internal stress and, in turn, blocks dislocations. Chan used the cosine function to describe periodic composition changes as [48]:

$$C - C_0 = A(\beta)\cos\beta \tag{4}$$

where C is elemental concentration, C_0 is the average elemental concentration, and $A(\beta)$ is the amplitude. The value for β is calculated as $\beta = 2\pi/\lambda$, where λ is the wavelength of elemental fluctuation. Using this equation, Chan calculated the relationship between yield stress and amplitude and between yield stress and wavelength. The results showed that yield stress increases with amplitude and wavelength as $\lambda A^2/2\pi$.

In step-aged samples of SA and MSA, our EDS results showed differences in fluctuation among all three elements (Fig. 6). Because of these fluctuation differences, the Vickers hardness of SA and MSA samples increased by 100% and 85%, respectively (Fig. 8a). Both the amplitude (A) and the wavelength (λ) of this fluctuation were greater in the MSA sample than in the SA (Fig. 7). As discussed above, decomposition accelerated by application of a 3 T magnetic field, which increased the wavelength and lowered the hardness (Figs. 7 and 8).

In order to study the hardness mechanism increased by spinodal decomposition, using the dislocation dynamics method, for {110} ⟨111⟩ and {112} <111> slip systems, Takahashi et al. studied the relationship between the increase of critical resolved shear stress (ΔCRSS) and amplitude (A) and wavelength (λ) of Fe-Cr alloys. Their results showed that, for both slip systems, the ΔCRSS increased almost linearly with amplitude increases. For the {110} <111> slip system, the ΔCRSS did not

Table 2
Lattice constant (nm) of SA and MSA samples, calculated using lattice spacing in (110), (−110), (010), and (100) directions.

Samples	(110)	Error bar	(−110)	Error bar	(010)	Error bar	(100)	Error bar	Average value
SA (in α_1)	0.2837	0.0019	0.2734	0.0031	0.2741	0.0013	0.2834	0.0015	0.2787
SA (in α_2)	0.2814	0.0043	0.2730	0.0023	0.2738	0.0010	0.2816	0.0005	0.2775
MSA (in α_1)	0.2756	0.0012	0.2744	0.0004	0.2787	0.0018	0.2750	0.0005	0.2759
MSA (in α_2)	0.2754	0.0008	0.2731	0.0005	0.2776	0.0009	0.2729	0.0011	0.2748

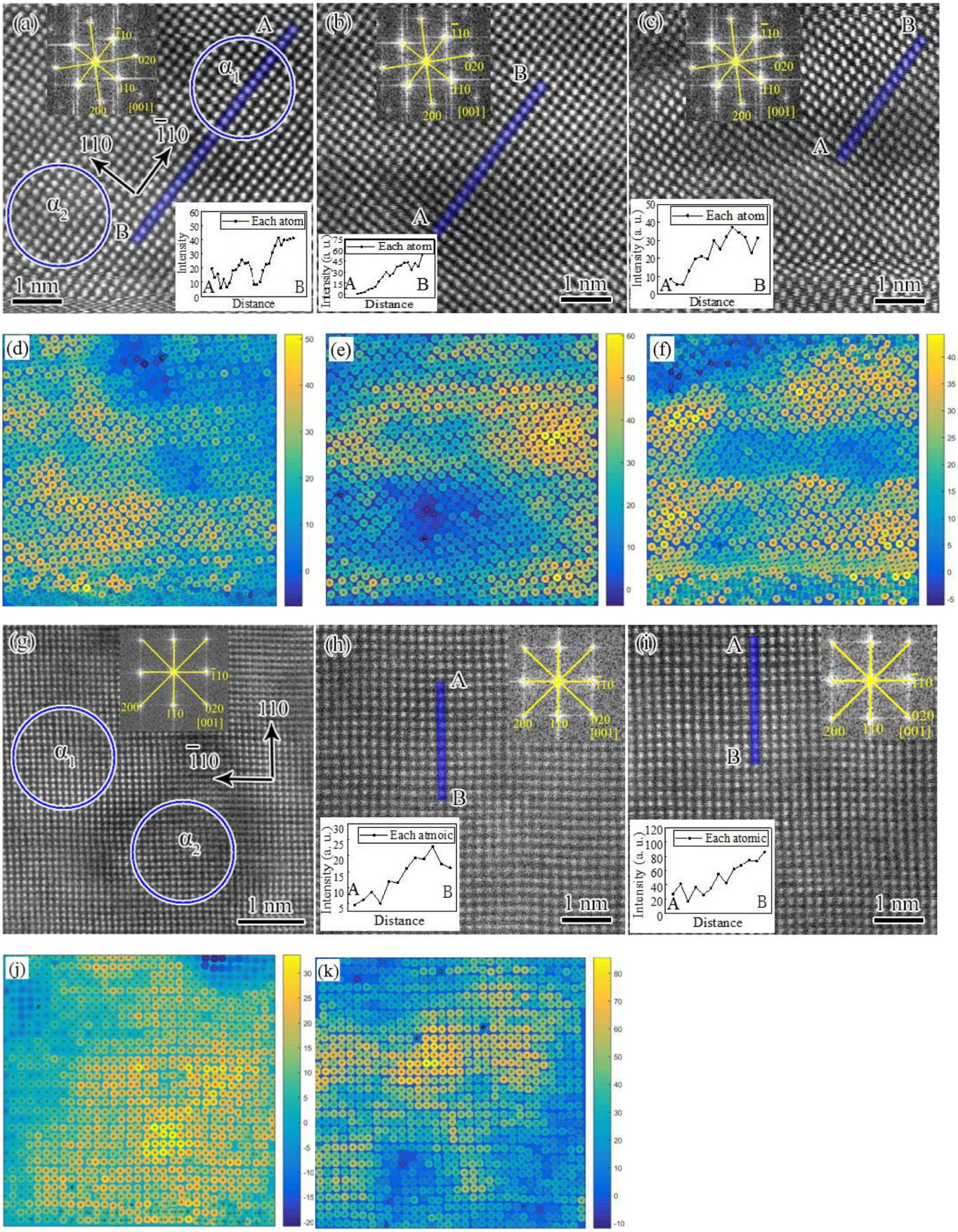
(a)
(b)
(c)
(d)
(e)
(f)
(g)
(h)
(i)
(j)
(k)
A
B
α_1
α_2
110
$\bar{1}10$
020
200
[001]
1 nm
Each atom
Each atmoic
Each atomic
Intensity
Intensity (a. u.)
Distance

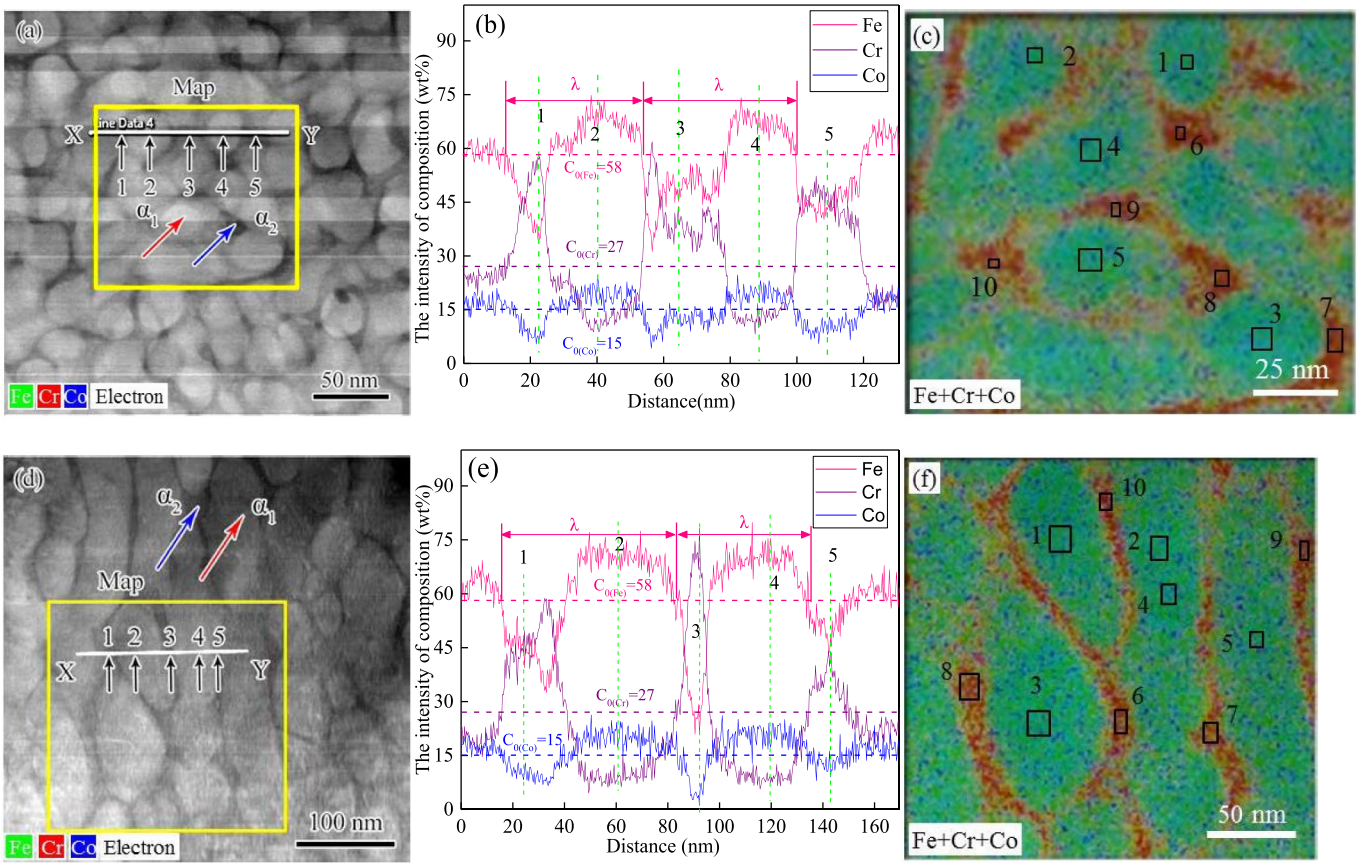

Fig. 6. HAADF/EDS data from samples designated as SA and MSA. Fig. 6a. HAADF image of α_1 and α_2 phases in SA samples. Yellow square corresponds to the area of EDS mapping, white line to the EDS line scan, and black arrows to the positions shown in Table 3 above. Fig. 6b. EDS line scan profile showing local composition (weight percent) of Fe (pink), Cr (purple), and Co (blue) along the line indicated in Fig. 6a. Composition at locations 1, 2, 3, 4, 5 is shown in Table 3. Fig. 6c. Overlay EDS map of Fe (green), Cr (red), and Co (blue) within the area delineated in Fig. 6a. by the yellow square. Fig. 6d. HAADF image of α_1 and α_2 phases in MSA samples. Fig. 6e. EDS line scan profile showing local composition (weight percent) of Fe (pink), Cr (purple), and Co (blue) along the white line indicated in Fig. 6d. Composition at locations 1, 2, 3, 4, 5 appears in Table 3. Fig. 6f. Overlay EDS map of Fe (green), Cr (red), Co (blue) in the area delineated in yellow square in Fig. 6d.

Table 3
The composition of each point of SA and MSA samples (wt%), each point indicated in Fig. 6b and e.

Samples	Point 1	Point 2	Point 3	Point 4	Point 5
SA	38Fe57Cr5Co	74Fe12Cr14Co	52Fe36Cr12Co	67Fe11Cr22Co	44Fe50Cr6Co
MSA	42Fe49Cr9Co	70Fe15Cr15Co	25Fe71Cr4Co	71Fe9Cr20Co	45Fe44Cr11Co

show a strong dependence on λ. However, for the {112} <111> slip system, the ΔCRSS dependence on λ was closely associated with the angle (θ) between a dislocation line and the Burgers vector. With θ = 90° and 39.2°, the ΔCRSS decreased when λ increased. For other angles, the ΔCRSS increased when λ increased [18]. Our hardness results are consistent with Takahashi's conclusions only when the edge dislocation and mixed dislocation (the angle (θ) between dislocation line and Burgers vector is 39.2°) moved in the {112} <111> slip system.

The ΔCRSS can be derived as follows [55]:

$$\Delta CRSS = A\eta Y/2 + 0.65\Delta Gb/\lambda \quad (5)$$

where $A\eta Y/2$ represents the misfit-hardening effect, and $0.65\Delta Gb/\lambda$ represents the modulus-hardening effect induced by composition variations, with A the amplitude, λ the wavelength, b the magnitude of the Burgers vector, and η the coefficient describing coherency strain induced by lattice misfit. The value for η is derived as follows [56]:

Fig. 5. Analysis of atomic resolution HAADF-STEM images of α_1 and α_2 phases of SA and MSA samples, as viewed along [001] direction. Variation in intensity corresponds to variation in composition between or within phases. Fig. 5a. Intensity variation from α_1 to α_2 in SA sample. Left bright region is α_1, right dark region is α_2. Bottom inset shows intensity profile of values taken along the blue line. Fig. 5b. Intensity variation within α_1 phase in SA sample. Bottom inset shows that the intensity ratio between bright and dark regions is about 6.9 ± 0.09 based on the intensity profile of values taken along the blue line. Fig. 5c. Intensity variation within α_2 phase of SA sample. Bottom inset shows that the intensity ratio between bright and dark is about 6.5 ± 0.2 based on the intensity profile of values taken from each atom along the blue line. Fig. 5d-f. Digitized images of the intensity variations shown in Fig. 5a-c. Each dot represents the integrated intensity of one atomic column, which undergoes smooth variation between columns. Fig. 5g. Intensity variation from α_1 to α_2 in MSA sample. Fig. 5h. Intensity variation within α_1 phase of SA sample. Bottom inset shows that the intensity ratio between bright and dark is about 5.1 ± 0.1, based on the intensity profile of values taken along the blue line. Fig. 5i. Intensity variation within α_2 phase of MSA sample. Bottom inset shows that the intensity ratio between bright and dark at about 5.3 ± 0.2 based on the intensity profile of values taken along the blue line. Fig. 5j-k. Digitized images of the intensity variations shown in Figs. 5h-i. Each dot represents the integrated intensity of one atomic column, which undergoes smooth variation between columns.

Table 4
The composition of each map of SA and MSA samples (wt%). The average compositions of α_1 for SA and MSA samples are 68.9Fe12Cr19.1Co and 70.6Fe9.1Cr20.3Co, respectively. The average compositions of α_2 for SA and MSA samples are 31.5Fe62Cr6.4Co and 31.6Fe62.4Cr6Co, respectively.

Samples	Maps in α_1 phase				
	Map 1	Map 2	Map 3	Map 4	Map 5
SA	70.6Fe11.5Cr17.9Co	69.3Fe10.6Cr20.1Co	68.3Fe12.7Cr19Co	68.5Fe11.9Cr19.6Co	67.8Fe13.5Cr18.7Co
MSA	71.5Fe8.5Cr20Co	69.5Fe9.7Cr20.8Co	72Fe7.7Cr20.3Co	68.9Fe7.9Cr23.2Co	71.2Fe11.7Cr17.1Co
Samples	Maps in α_2 phase				
	Map 6	Map 7	Map 8	Map 9	Map 10
SA	30Fe63.5Cr6.5Co	31Fe64.5Cr4.5Co	32.5Fe61.7Cr5.8Co	32.8Fe59.8Cr7.3Co	31.4Fe60.6Cr8Co
MSA	30.1Fe63.8Cr6.1Co	34.5Fe59.3Cr6.2Co	33.2Fe61Cr5.8Co	31.5Fe62.6Cr5.8Co	28.7Fe65.2Cr6.1Co

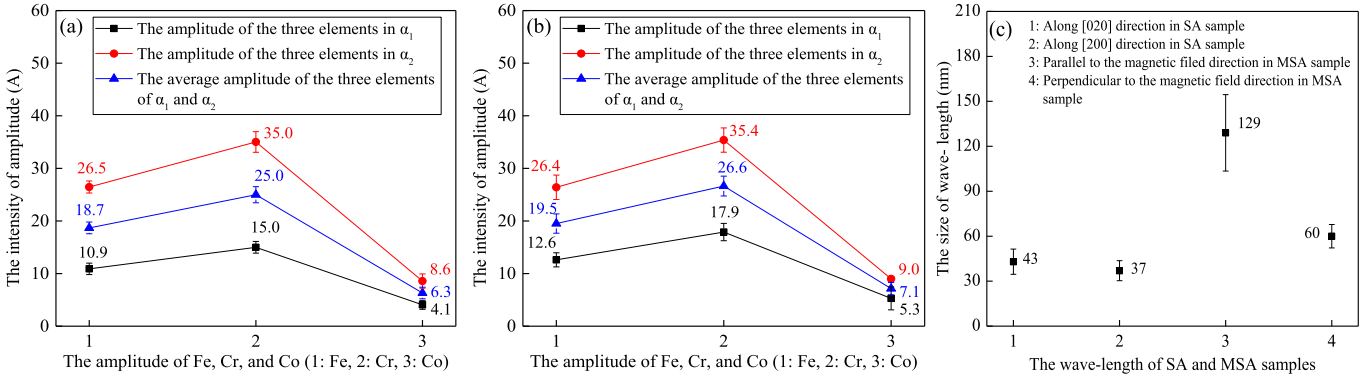

Fig. 7. The amplitude of Fe, Cr, Co and the wavelength of element fluctuation of SA and MSA samples. Before step aging, the original concentrations of Fe, Cr, and Co were 58wt%, 27%wt%, and 15%wt%, respectively. In both types samples, we measured 1, 2, 3, 4, 5 EDS maps to analyze the amplitude of the three elements in α_1, and 6, 7, 8, 9, 10 EDS maps to analyze the amplitude of the three elements in α_2. We also analyzed the average amplitude of two phases for each sample (also see Table 4). (a) The amplitude of three elements in α_1 and α_2 phases, and the average for SA sample. (b) The amplitude of three elements in α_1 and α_2 phases, and the average for MSA sample. (c) The wavelength of element fluctuation of SA and MSA samples.

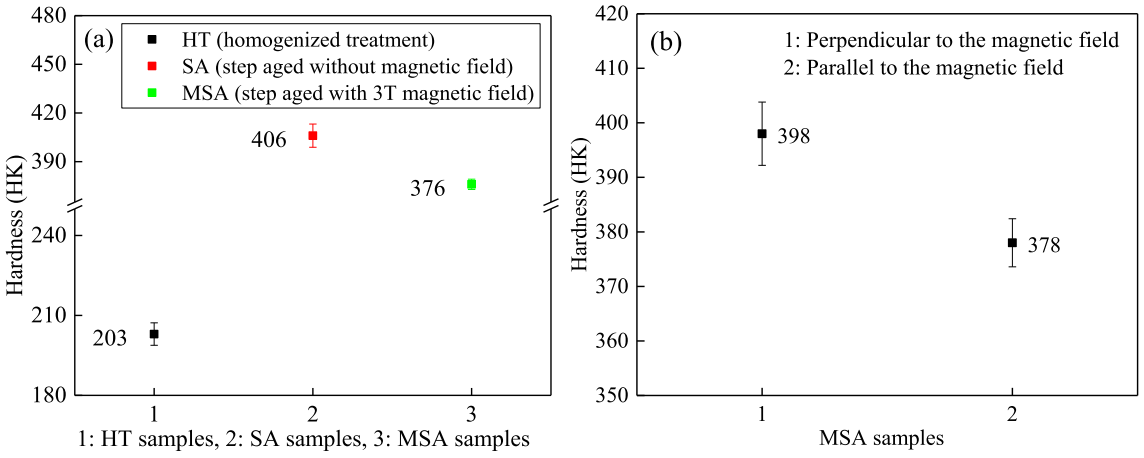

Fig. 8. Hardness of HT, SA, and MSA samples. (a) Vickers hardness of the three samples. (b) Knoop hardness of MSA sample in two directions: parallel and perpendicular to the magnetic direction.

$$\eta = \frac{\Delta a}{2Aa_0} \tag{6}$$

where a is the lattice constant. The elastic constant, Y, is derived as follows:

$$Y = \frac{E}{1-\nu} \tag{7}$$

where E is Young's modulus, and ν is Poisson's ratio. The amplitude of shear modulus change, ΔG, is derived as follows:

$$\Delta G = \frac{\Delta C}{G_A - G_B} \tag{8}$$

where ΔC is the composition difference of element Z between *Z*-rich and Z-poor regions, G_A and G_B are the shear moduli of elements A and B, respectively.

For Fe-Cr-Co ternary alloys, the ΔCRSS can be derived using the following equation:

Table 5
The parameters of η, ν, E, Y, $\Delta C_{Fe\text{-}Cr}$, $\Delta C_{Fe\text{-}Co}$, $\Delta G_{Fe\text{-}Cr}$, $G_{Fe\text{-}Co}$, (Fe-Cr) vol. %, and (Fe-Co) vol. % for SA and MSA samples.

Samples	η	ν	E (GPa)	Y (GPa)	$\Delta C_{Fe\text{-}Cr}$ (GPa)	$\Delta C_{Fe\text{-}Co}$ (GPa)	$\Delta G_{Fe\text{-}Cr}$ (GPa)	$\Delta G_{Fe\text{-}Co}$ (GPa)	(Fe-Cr) vol. %	(Fe-Co) vol. %
SA	0.0086	0.331	229	342	0.5	0.13	16.50	0.78	69%	31%
MSA	0.0075	0.331	229	342	0.53	0.143	17.49	0.858	69%	31%

$$\Delta CRSS_{Fe-Cr-Co} = ((Fe-Cr)vol.\%)\Delta CRSS_{Fe-Cr} + ((Fe-Co)vol.\%)\Delta CRSS_{Fe-Co} \quad (9)$$

We estimated the ΔCRSS for our binary alloys by substituting A with A_{Cr} and A_{Co}, and ΔG with $\Delta G_{Fe\text{-}Cr}$ and $\Delta G_{Fe\text{-}Co}$ in Eq. (5):

$$\Delta CRSS_{Fe-Cr} = A_{Cr}\eta Y/2 + 0.65\Delta G_{Fe-Cr}b/\lambda \quad (10)$$

$$\Delta CRSS_{Fe-Co} = A_{Co}\eta Y/2 + 0.65\Delta G_{Fe-Co}b/\lambda \quad (11)$$

For both Cr and Co, composition amplitudes varied between α_1 and α_2. For our calculations, we used the mean value of amplitude for each phase. In the SA sample, the mean amplitudes of Cr and Co were 0.25 and 0.063, respectively. In the MSA sample, the mean amplitudes of Cr and Co were 0.266 and 0.071, respectively. In the SA sample, the average wavelength along the [200] and [020] directions was 40 nm, whereas in the MSA sample, the average wavelength in the directions parallel and perpendicular to the magnetic field was 95 nm (Fig. 7).

The value of b in the above equations was 2.5×10^{-10} m in Fe-Cr alloys [55], and we used this value for our calculations. We used average lattice constants of α_1 and α_2 phases to calculate the η for SA and MSA samples (Tables 2 and 5). The values of the Young's modulus for Fe, Cr, and Co are 211 GPa, 279 GPa, and 209 GPa, respectively and were used to estimate the Young's modulus of Fe27wt%Cr15wt%Co (Table 5). The shear modulus of Fe, Cr, and Co are 82 GPa, 115 GPa, and 76 GPa, respectively. We also calculated the values of Y, $\Delta C_{Fe\text{-}Cr}$, $\Delta C_{Fe\text{-}Co}$, $\Delta G_{Fe\text{-}Cr}$, $\Delta G_{Fe\text{-}Co}$ (Table 5). We estimated the volume fraction of Fe-Cr and Fe-Co for the two samples (Table 5).

With the above values in Tables 2 and 5 for Eqs. (9), (10), and (11) we estimate $\Delta CRSS_{Fe\text{-}Cr\text{-}Co}$. For SA and MSA samples, ΔCRSS was about 330 MPa and 285 MPa, respectively, and the ΔCRSS ratio between the two samples was 1.16.

The relationship between hardness (HV) and tensile strength (σ_y) has been described by [57]:

$$HV = C_{h\nu/\upsilon y} \times \sigma_y \quad (12)$$

where $C_{h\nu/\upsilon y}$ is a constant that is dependent on the materials tested and the geometry of the indenter. The value for $C_{h\nu/\upsilon y}$ is about 0.306 for steels. After step aging, the increase in hardness (HV) was 203 for SA and 173 for MSA samples (Fig. 8). The increase in tensile strength (MPa) was 663 for SA and 565 for MSA samples. Under the Von Mises criterion, the relationship between shear strength and tensile strength is 0.5 for metals. Thus, shear strength values would be about 332 MPa for SA and 283 MPa for MSA samples and the shear strength ratio of SA over MSA samples would be 1.17. This value was consistent with our calculations based on Eqs. (9), (10), and (11).

In SA and MSA samples, the estimated deformation zones introduced by the indenter were about 762 and 930 μm^2, respectively, and the area ratio between deformation zones and indentation zones was about 0.29 for SA and 0.32 for MSA samples (Fig. 9). This indicates that the ductility was greater in MSA than in SA samples.

Our Knoop hardness test results indicated anisotropy in all samples, consistent with the anisotropy of the composition wavelength resulting from spinodal decomposition (see appendix B).

4. Conclusions

Spinodal decomposition resulted in improved microstructure and hardness of Fe-27wt%Cr-15wt%Co. Our major results are as follows:

(1) Lattice constants increased after step aging in a 3 T magnetic field, but they increased even more without magnetic field.
(2) After step aging, the α phase decomposed into Fe-Co rich α_1 and Cr rich α_2. In samples step aged without magnetic field, spherical α_1 domains were interspersed through the surrounding α_2 network. After step aging at 3 T, however, elongated α_1 domains lined up parallel to the direction of the magnetic field against the background of surrounding α_2 network. The overall composition

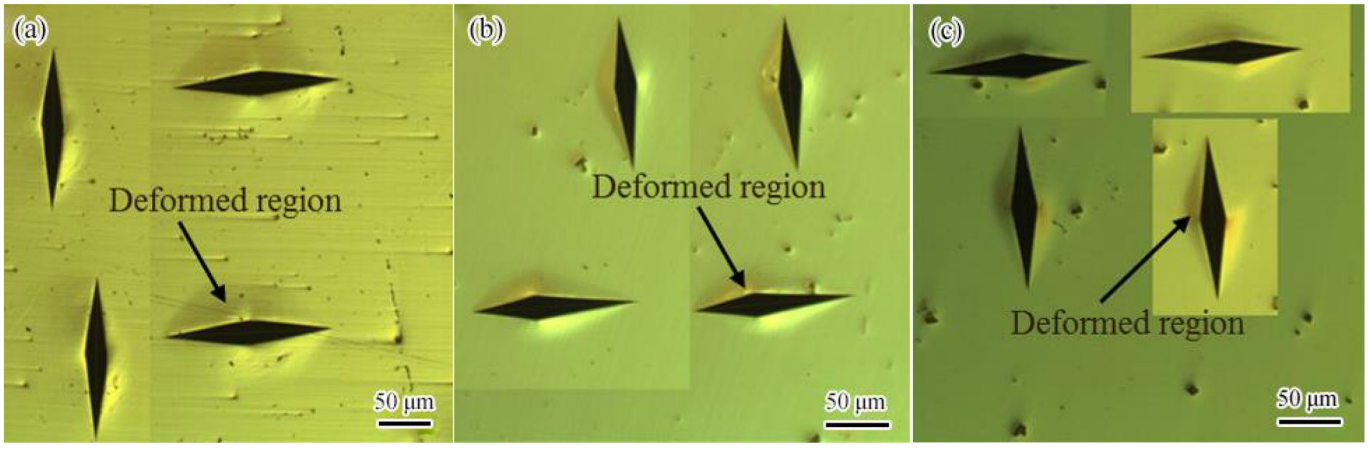

Fig. 9. Analysis of the area of deformed region of HT, SA, and MSA samples. (a) The image of deformed region introduced by indenter of HT sample. (b) The image of deformed region introduced by indenter of SA sample. (c) The image of deformed region introduced by indenter of MSA sample. We measured the area of deformed region of Types HT, SA, and MSA samples are 5591 ± 1190 μm^2, 762 ± 91 μm^2, and 930 ± 98 μm^2, respectively.

of the alloy gradually changed from α_1 to α_2, indicating no sharp interface between the two phases. Fe, Cr and Co were inhomogeneously distributed inside each phase, indicating that fine-scale spinodal decomposition had occurred.

(3) After step aging, the changes that occurred in Fe, Cr, or Co conformed to the cosine function in that each of the elements had its own amplitude (A) and wavelength (λ). Concentrations of Fe and Co reached their peaks in the α_1 phase and their valleys in α_2 phase. By contrast, the concentration of Cr reached its peak in the α_2 phase and its valley in α_1 phase. Application of a 3 T magnetic field increased both amplitude and wavelength for all three elements.

(4) After step aging, the hardness increased due to spinodal decomposition. Application of a 3 T magnetic field during step aging coarsened the microstructure, decreased hardness, and increased toughness. The magnetic field induced an anisotropy in the hardness, which was greater in the direction perpendicular to the magnetic field.

CRediT authorship contribution statement

Zhaolong Xiang: Conceptualization, Writing - original draft, Writing - review & editing, Methodology, Visualization, Investigation. **Lin Zhang:** Conceptualization, Resources, Methodology, Writing - review & editing. **Yan Xin:** Writing - review & editing, Resources, Validation, Investigation. **Bailing An:** Validation, Investigation. **Rongmei Niu:** Resources, Validation, Investigation. **Masoud Mardani:** Resources, Investigation. **Theo Siegrist:** Writing - review & editing, Resources, Validation. **Jun Lu:** Resources, Validation. **Robert E. Goddard:** Resources, Investigation. **Tiannan Man:** Writing - review & editing. **Engang Wang:** Conceptualization, Resources, Methodology, Writing - review & editing, Supervision, Project administration, Funding acquisition. **Ke Han:** Conceptualization, Resources, Methodology, Writing - review &editing, Supervision, Project administration, Funding acquisition, Validation.

Declaration of Competing Interest

The authors declare that they have no known competing financial interests or personal relationships that could have appeared to influence the work reported in this paper.

Acknowledgement

This work was supported by the National Natural Science Foundation of China (51674083 and No. U1760206) and the 111 Project (2.0) of China (BP0719037). A portion of this work was performed at the National High Magnetic Field Laboratory (NHMFL), which is supported by National Science Foundation (Cooperative Agreement No. DMR-1157490 and DMR-1644779) and the State of Florida. Zhaolong Xiang and Bailing An were supported by China Scholarship Council (CSC). The authors are also thankful to Dr. Mary Tyler for editing.

Appendix A. Appendix

Table A.1. Lattice spacing (nm) of SA (step aged without magnetic field) and MSA (step aged with 3 T magnetic field) samples at (−110), (110), (010), and (100) directions.

Samples	(110)	(−110)	(010)	(100)
SA (in α_1)	0.1933	0.2013	0.2844	0.2741
SA II (in α_2)	0.1931	0.1989	0.2816	0.2738
MSA (in α_1)	0.1947	0.1956	0.2752	0.2787
MSA (in α_2)	0.1931	0.1947	0.2729	0.2776

The Knoop hardness test of HT sample (homogenized treatment) showed that the hardness value was smaller when the indenter was parallel to the cooling direction rather than perpendicular. This may be related to the grain size parallel to the cooling direction was larger than perpendicular (Fig. B.1). The Knoop hardness value for SA sample (step aged without magnetic field) was greater when the indenter was parallel to the cooling direction (parallel to the magnetic field) rather than perpendicular (Fig. B.2). This may be related to the wave-length (λ) of element fluctuation was different in different direction. However, the Knoop hardness value for MSA (step aged with 3 T magnetic field) was smaller when the indenter was parallel to the magnetic field rather than perpendicular (Fig. B.2). This indicated that the wave-length was greater in the direction of the magnetic field. The Knoop hardness tests showed the anisotropy in hardness resulting from amplitude (A) and wavelength (λ) anisotropy.

Appendix B. Appenix

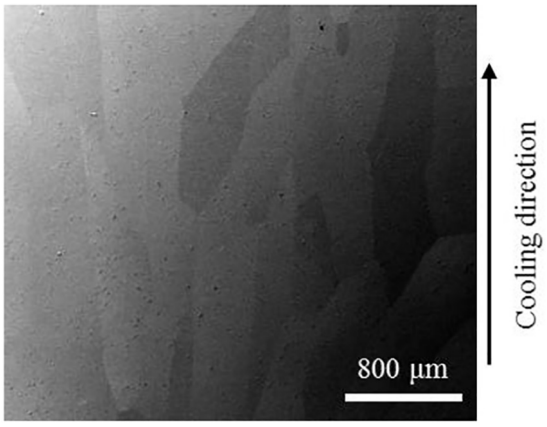

Fig. B.1 SEM image of HT sample. The average grain sizes of parallel and perpendicular to the cooling direction are 1034 ± 420 μm and 257 ± 81 μm, respectively.

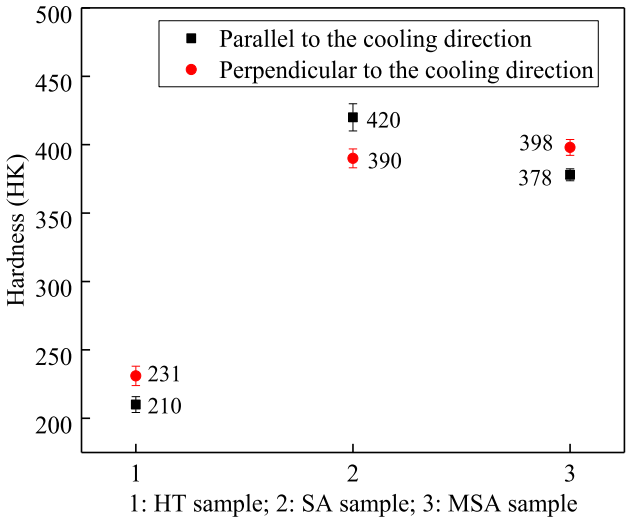

Fig. B.2. Knoop hardness of the HT, SA, and MSA samples in two directions: parallel and transverse to the cooling direction (The cooling direction is parallel to the direction of 3 T magnetic field).

References

[1] T. Suzudo, H. Takamizawa, Y. Nishiyama, A. Caro, T. Toyama, Y. Nagai, J. Nucl. Mater. 540 (2020) 152306.
[2] X.H. Han, S.J. Bu, X. Wu, J.B. Sun, Y. Zhang, C.X. Cui, J. Alloys Compd. 694 (2017).
[3] S. Sugimoto, M. Okada, M. Homma, J. Appl. Phys. 63 (1988) 3707–3709.
[4] E.V. Belozerov, N.V. Mushnikov, G.V. Ivanova, N.N. Shchegoleva, V.V. Serikov, N.M. Kleinerman, A.V. Vershinin, M.A. Uimin, Phys. Met. Metallogr. 113 (2012) 319–325.
[5] S.I. Stel'mashok, I.M. Milyaev, V.S. Yusupov, A.I. Milyaev, Met. Sci. Heat Treat. 58 (2017) 622–627.
[6] H. Zijlstra, IEEE Trans. Magn. 14 (1978) 661–664.
[7] P. Jia, J.M. Liu, E.G. Wang, K. Han, J. Alloys Compd. 581 (2013) 373–377.
[8] X. Duan, C. Wu, X.Y. Wang, X.M. Tian, W.L. Pei, K. Wang, Q. Wang, J. Alloys Compd. 797 (2019) 1372–1377.
[9] D. Zhao, X.Y. Wang, L. Chang, W.L. Pei, C. Wu, F. Wang, L.R. Zhang, J.J. Wang, Q. Wang, J. Mater. Sci. Technol. 73 (2021) 178–185.
[10] L. Zhang, K. Han, X.R. Zhang, E.G. Wang, J. Lu, R. Goddard, J. Magn. Magn. Mater. 490 (2019) 165533.
[11] M. Altafi, E. Mohammad Sharifi, A. Ghasemi, J. Magn. Magn. Mater. 507 (2020) 166837.
[12] M. Okada, R. Togashi, S. Sugimoto, M. Homma, J. Appl. Phys. 64 (1988) 5732–5734.
[13] X.H. Tan, S.F. Chan, K. Han, H. Xu, Sci. Rep. 4 (2014) 1–5.
[14] D.R. Brown, K. Han, T. Siegrist, T. Besara, R.M. Niu, AIP Adv. 6 (2016) 1–8.
[15] R.A. Rastabi, A. Ghasemi, M. Tavoosi, M. Ramazani, J. Magn. Magn. Mater. 426 (2017) 744–752.
[16] T.S. Chin, T.S. Wu, C.Y. Chang, T.K. Hsu, Y.H. Chang, J. Mater. Sci. 18 (1983) 1681–1688.
[17] S. Jin, S. Mahajan, D. Brasen, Metall. Mater. Trans. A 11 (1980) 69–76.
[18] A. Takahashi, T. Suzuki, A. Nomoto, T. Kumagai, Acta Mater. 146 (2018) 160–170.
[19] O. Soriano-Vargas, E.O. Avila-Davila, V.M. Lopez-Hirata, N. Cayetano-Castro, J.L. Gonzalez-Velazquez, Mater. Sci. Eng. A 527 (2010) 2910–2914.
[20] O. Soriano-Vargas, E.O. Avila-Davila, V.M. Lopez-HiratLopez-Hirata, H.J. Dorantes-Rosales, J.L. Gonzalez-Velazquez, Mater. Trans. 50 (2009) 1753–1757.
[21] X. Xu, J.E. Westraadt, J. Odqvist, T.G.A. Youngs, S.M. King, P. Hedström, Acta Mater. 145 (2018) 347–358.
[22] F. Danoix, P. Auger, D. Blavette, Microsc. Microanal. 10 (2004) 349–354.
[23] K.H. Park, J.C. LaSalle, L.H. Schwartz, M. Kato, Acta Metall. 34 (1986) 1853–1865.
[24] H. Kaneko, M. Homma, K. Nakamura, M. Okada, G. Thomas, IEEE Trans. Magn. 13 (1977) 1325–1327.
[25] M.E. Houghton, P.L. Rossiter, P.E. Clark, J. Mater. Sci. 13 (1978) 155–166.
[26] N.M. Kleinerman, E.V. Beloserov, N.V. Mushnikov, V.V. Serikov, J. Phys. Conf. Ser. 217 (2010) 8–12.
[27] M.I. Alymov, I.M. Milyaev, A.E. Sychev, D.Y. Kovalev, V.P. Korneev, Y.G. Morozov, V.S. Yusupov, T.A. Bompe, Russ. Metall. 2014 (2014) 555–560.
[28] Z.L. Xiang, L. Zhang, M.H. Huang, X.R. Zhang, P. Jia, E.G. Wang, Rare Metal Mater. Eng. 46 (2017) 3532–3537 (In Chinese).
[29] L. Zhang, Z.L. Xiang, X.D. Li, E.G. Wang, Nanomaterials 8 (2018) 1–14.
[30] S. Tao, Z. Ahmad, I.U. Khan, P.Y. Zhang, X.M. Zheng, J. Magn. Magn. Mater. 469 (2019) 342–348.
[31] Z. Ahmad, A. Ul Haq, S.W. Husain, T. Abbas, Phys. B Condens. Matter 321 (2002) 96–103.
[32] R.C. Murty, Nature 207 (1965) 239–399.
[33] T. Malis, S.C. Cheng, R.F. Egerton, Microsc. Res. Tech. (1988) 193–200.
[34] K.E. Macarthur, L.B. Jones, S. Lozano-Perez, D. Ozkaya, P.D. Nellist, J. Phys. Conf. Ser. 522 (2014).
[35] L. Jones, K.E. Macarthur, V.T. Fauske, A.T.J. Van Helvoort, P.D. Nellist, Nano Lett. 14 (2014) 6336–6341.
[36] S.I. Kondo, A. Masusaki, K. Ogawa, T. Morimura, H. Nakashima, Nippon Kinzoku Gakkaishi/J. Jpn. Inst. Met. 79 (2015) 664–671.
[37] S.I. Kondo, H. Nakashima, T. Morimura, Phys. B Condens. Matter 560 (2019) 244–254.
[38] N. Debnath, T. Kawaguchi, W. Kumasaka, H. Das, K. Shinozaki, N. Sakamoto, H. Suzuki, N. Wakiya, J. Magn. Magn. Mater. 432 (2017) 391–395.
[39] M. Kheradmandfard, S.F. Kashani-Bozorg, K.H. Kang, O.V. Penkov, A. Zarei Hanzaki, Y.S. Pyoun, A. Amanov, D.E. Kim, J. Alloys Compd. 738 (2018) 540–549.
[40] X.F. Meng, W. Cai, Z.H. Liu, J. Li, H.Y. Geng, J.H. Sui, Acta Mater. 98 (2015) 405–415.
[41] J. Hao, Y.D. Zhang, P. Ren, K. Zhang, J.H. Chen, S.X. Du, M.J. Wang, M. Wen, Ceram. Int. 44 (2018) 21358–21364.
[42] Y. Muraoka, F. Yoshii, T. Fukuda, Y. Manabe, M. Yasuno, Y. Takemoto, K. Terashima, T. Wakita, T. Yokoya, Thin Solid Films 698 (2020) 1–2.
[43] Y. Matsuura, F. Yoshii, T. Otsuka, K. Kadowaki, M. Ijiri, Y. Takemoto, K. Terashima, T. Wakita, T. Yokoya, Y. Muraoka, J. Eur. Ceram. Soc. 38 (2018) 5043–5050.
[44] J.C. Zhao, M.R. Notis, Acta Mater. 46 (1998) 4203–4218.
[45] Y. Belli, M. Okada, G. Thomas, M. Homma, H. Kaneko, J. Appl. Phys. 49 (1978) 2049–2051.
[46] X.Y. Sun, C.Y. Xu, L. Zhen, L.X. Lv, L. Yang, J. Magn. Magn. Mater. 312 (2007) 342–346.
[47] H. Kaneko, M. Homma, M. Okada, S. Nakamura, N. Ikuta, AIP Conf. Proc. 620 (1976) 620–621.
[48] J.W. Chan, Acta Metall. 11 (1963).
[49] Y.Y. Ren, H.H. Yao, J.H. Hu, G.Q. Cao, J.J. Tian, J.M. Pan, Scr. Mater. 187 (2020) 107–112.
[50] T.K. Yao, A.R. Wagner, X. Liu, A. EI-Azab, J.M. Harp, J. Gan, D.H. Hurley, M.T. Benson, L.F. He, Materialia 9 (2020) 100592.
[51] X.H. Han, J.B. Sun, H.W. Wang, Z.X. Dong, Y. Zhang, C.X. Cui, J. Alloys Compd. 806 (2019) 1188–1199.
[52] T. Nishizawa, M. Hasebe, M. Ko, Acta Metall. 27 (1979) 817–828.
[53] Y.P. Tang, W. Goto, S. Hirosawa, Z. Horita, S. Lee, K. Matsuda, D. Terada, Acta Mater. 131 (2017) 57–64.
[54] J.Z. Yan, N. Li, X. Fu, Y. Zhang, Mater. Sci. Eng. A 618 (2014) 205–209.
[55] M. Kato, Acta Metall. 29 (1981) 79–87.
[56] R. Wagner, J. Phys. B 31 (1981) 198–208.
[57] K. Han, D.V. Edmonds, G.D.W. Smith, Metall. Mater. Trans. A Phys. Metall. Mater. Sci. 32 (2001) 1313–1324.